nature communications

Article

https://doi.org/10.1038/s41467-025-64389-9

Photocatalytic non-oxidative dehydrogenation of ethane to ethene with near unit selectivity

Received: 16 January 2025

Accepted: 15 September 2025

Published online: 23 October 2025

Check for updates

Xiaoyu Sui[1,2,6], Jiwu Zhao[1,2,6], Pu Zhang[1,2,6], Ying Wang[1,2] ✉, Hangbin Zheng[1,2], Haihua Zeng[1,2], Pengzhao Wang[3], Yanyan Jia[4], Na Wen[5], Zhengxin Ding[1,2], Zizhong Zhang[1,2], Sheng Dai[4], Chao Xu[1,2], Rusheng Yuan[1,2], Wenxin Dai[1,2], Xianzhi Fu[1,2] & Jinlin Long[1,2] ✉

The non-oxidative dehydrogenation of light alkanes to alkenes is thermodynamically limited by the trade-off between the cleavage of C-H and C-C bonds. Unlocking the thermodynamic bottleneck with photocatalysis is prone to eliminate undesirable side reactions such as deep dehydrogenation, cracking, isomerization, and polymerization. Herein, we show the photocatalytic non-oxidative dehydrogenation of ethane to ethene and hydrogen at ambient conditions, which is enabled by grafting of Ni single atoms to modulate the surface electronic structure of Pd nanoparticles photo-deposited on the surface of anatase TiO_2 nanoparticles, modifying the ethane dehydrogenation pathway. A high rate of 8.2 ± 0.2 mmol·g^{-1}·h^{-1} for the stoichiometric conversion of ethane to ethene and hydrogen is achieved with a 100% ethene selectivity in a flow reactor under solar light irradiation. The apparent quantum efficiency reaches ~22.3% at 350 nm by using the optimal T-$Ni_{0.6}Pd_{0.24}$ photocatalyst. Solar-driven non-oxidative alkane dehydrogenation offers a route to light alkenes with high performance, and selectivity.

Ethene (C_2H_4) is one of the largest basic organic chemical raw materials in terms of production and consumption worldwide, often referred to as the blood of the petrochemical industry[1]. The traditional method for ethene production is the steam cracking of naphtha[2,3], which requires the use of severe high-temperature (800 °C–1000 °C), high-pressure reaction conditions[4]. With the emergence of shale gas, its development and utilization have become a hot topic in the global energy field[5,6]. Among them, the catalytic dehydrogenation of ethane (C_2H_6, the second most abundant component in shale gas) to produce ethene has attracted wide attention due to its low cost and energy consumption[7,8]. Currently, the ethane dehydrogenation (EDH) reactions are generally classified into two categories: oxidative ethane dehydrogenation (OEDH) and non-oxidative ethane dehydrogenation (NOEDH). Although OEDH ($C_2H_6 + 1/2O_2 \rightarrow C_2H_4 + H_2O$, $\Delta H^{\theta}_{298\ K} = -105$ kJ mol^{-1}) is thermodynamically more favorable, the excessive oxidation occurs often, resulting in the production of CO_2 and CO due to the higher reactivity of generated ethene compared to the reactant ethane[9–11]. Compared with OEDH, NOEDH ($C_2H_6 \rightarrow C_2H_4 + H_2$, $\Delta H^{\theta}_{298\ K} = +136.5$ kJ mol^{-1}) has unique advantages in avoiding overoxidation and producing valuable ethene and hydrogen fuel[12,13].

Although several metals like Pt, Cr, and Ga were often used as industrial catalysts for dehydrogenation reactions[14], especially

[1]State Key Laboratory of Chemistry for NBC Hazards Protection, College of Chemistry, Fuzhou University, Fuzhou, P. R. China. [2]State Key Laboratory of Photocatalysis on Energy and Environment, College of Chemistry, Fuzhou University, Fuzhou, P. R. China. [3]College of Chemical Engineering, Fuzhou University, Fuzhou, P. R. China. [4]Key Laboratory for Advanced Materials and Feringa Nobel Prize Scientist Joint Research Center, Institute of Fine Chemicals, School of Chemistry & Molecular Engineering, East China University of Science and Technology, Shanghai, P. R. China. [5]College of Materials Science and Engineering, Fuzhou University, Fuzhou, P. R. China. [6]These authors contributed equally: Xiaoyu Sui, Jiwu Zhao, Pu Zhang. ✉e-mail: ywang@fzu.edu.cn; jllong@fzu.edu.cn

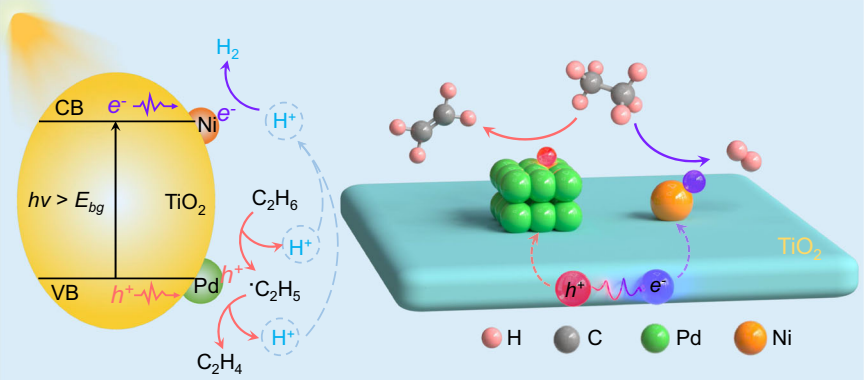

Fig. 1 | Design principle of dual metal sites modified semiconductor photocatalysts for solar alkene production. The elements H, C, Pd, and Ni are represented by pink, gray, green, and orange balls, respectively.

propane dehydrogenation to propene[15–17], EDH is more difficult due to its relatively high inertness. Activating the first hydrogen atom in ethane needs an energy of 415.3 kJ/mol, larger than the dissociation energy of the sp^3-C-H bonds in propane (401.3 kJ mol^{-1})[18]. Owing to the low dissociation energy of the C-C bond (345.6 kJ mol^{-1}), ethane is more prone to cleavage of C-C bond to form CH_4, instead of ethene, as a result, the deep dehydrogenation and unfavorable carbon deposition are easily occurred over metal catalysts, resulting in poor catalyst durability[19,20]. The intrinsic characteristics present significant challenges in achieving stoichiometric conversion of ethane to ethene and H_2 by classical catalytic processes.

Using solar energy to drive catalytic dehydrogenation reactions is a promising strategy to produce ethene under mild conditions. In contrast to thermochemically-driven catalytic processes operated in the electronic ground state, the photocatalytic process operated in the excited state to enable the selective destruction of the sp^3-C-H bonds in cycloalkanes by photogenerated electron-hole pairs[8,21]. A few recent studies showed that several Pd or Pt-loaded oxides were photocatalytically active for the OEDH reaction performed commonly using dioxygen and CO_2 as oxidants[22,23]. The ZnPd-supported ZnO photocatalyst reported by Zhang and co-workers gave a benchmark ethene production rate of 46.4 $mmol{\cdot}g^{-1}{\cdot}h^{-1}$ with 92.6% ethene selectivity in a fixed-bed flow reactor under 365 nm irradiation[18]. In contrast to Pd-based catalysts, gold-containing catalytic systems, such as Au/Ga_2O_3 and Au/TiO_2 exhibit preferential activation of C-C coupling pathways, resulting in the formation of higher hydrocarbons, whereas non-oxidative dehydrogenation (NODH) processes are markedly suppressed as a side pathway[24]. This distinct mechanistic divergence highlights the metal-specific reactivity governing hydrocarbon transformation. Beyond the identity of metallic species, the precise metal loading within catalytic systems also has a profound impact on the modulation of reaction pathways. Li et al. observed that when the Pd loading on a TiO_2 substrate was reduced below 0.5 wt%, the catalyst exhibited direct photocatalytic dehydrogenation behavior[25]. Under UV irradiation, H_2 production was significantly higher than C_2H_4 production. Conversely, Zhang et al. demonstrated that when the Pd loading on TiO_2 exceeded 0.5 wt%, it enabled a transition from non-oxidative to oxidative dehydrogenation[26]. Notably, in the case of NODH, the large thermodynamic barriers made the desorption of ethene from the surface of Pd ensembles difficult[27], forming overoxidized products and cokes and thus severely diminishing the yield and selectivity of C_2H_4. Ozin and co-workers proposed a photo-thermo-catalytically synergistic strategy to break the thermodynamic bottleneck, and demonstrated the efficient ethene production via the photochemically-driven NOEDH reaction over $LaMn_{1-x}Cu_xO_3$. An impressive ethene production rate of ~1.1 $mmol{\cdot}g^{-1}{\cdot}h^{-1}$ was achieved in a quartz fixed-bed reactor with 4.8 W cm^{-2} light intensity at 450 °C[3]. These findings highlight the paradigm-shifting potential of strategically engineering catalyst architectures for the enhancement of molecular selectivity through precision-guided pathway modulation, while reinforcing catalyst duration.

Herein, we design a single-atom (SA) Ni grafted Pd/TiO_2 photocatalyst for the efficient ethene production via the simulated solar light-driven NOEDH reaction at ambient conditions. The photocatalysts denoted as T-Ni_xPd_y (where T denotes TiO_2, x and y represent the weight percentages of Ni and Pd, respectively) are prepared by a combined procedure of surface organometallic chemistry (SOMC) of nickelocene ($Ni(C_5H_5)_2$) with photo-deposition of Pd nanoparticles (NPs)[26,28,29]. The grafted Ni SAs and deposited Pd NPs serve as electron-accepting sites for reducing protons to H_2 and as hole-accepting sites for cleaving C-H bonds, respectively, as depicted in Fig. 1. Unlike conventional single-metal Pd/TiO_2 systems, grafting Ni SAs on the surface of anatase TiO_2 NPs modifies the pathway of Pd-catalyzed EDH, weakening the adsorption of ethene on the surface of Pd NPs to accelerate the escape of ethene, as a result, the deep dehydrogenation and coke production are avoided eventually, and the charge-driven photoredox reactions are balanced kinetically. The reaction pathways are investigated using density functional theory (DFT) calculations and isotopic labeling experiments. In situ electron paramagnetic resonance (EPR) spectroscopy and in situ Fourier transformation infrared (FTIR) spectroscopy are conducted to explore the formation of key reactive intermediates.

Results and Discussion

Photocatalyst preparation and characterizations

Supplementary Fig. 1 illustrates the preparation procedure details of the T-Ni_x, T-Pd_y, and T-Ni_xPd_y samples. Firstly, a series of T-Ni_x samples with different Ni contents are synthesized by chemically grafting $Ni(C_5H_5)_2$ on the surface of anatase TiO_2 NPs, and its synthesis process was monitored by FTIR spectroscopy (Supplementary Fig. 2). A series of T-Pd_y samples with different Pd loadings are prepared on TiO_2 NPs by the photo-deposition method. By assessing the activity of T-Ni_x and T-Pd_y samples for the simulated solar light-driven NOEDH reaction (Supplementary Fig. 3), it is sure that the optimal contents of Ni and Pd are equal to 0.6 and 0.24 wt.%, respectively. Finally, 0.24 wt% Pd is photo-deposited onto the pre-optimized T-$Ni_{0.6}$ sample synthesized by SOMC, and the resulting sample is named T-$Ni_{0.6}Pd_{0.24}$. The X-ray powder diffraction (XRD) and transmission electron microscopy (TEM) characterizations indicate that after grafting Ni species and depositing Pd NPs, no diffraction peaks belonging to Ni, Pd species or other impurity phases are detected in the as-prepared T-$Ni_{0.6}Pd_{0.24}$ sample, and no any changes in crystal size and morphology of anatase TiO_2 NPs are discernable (Supplementary Figs. 4–6). The high-angle annular dark-

https://doi.org/10.1038/s41467-025-64389-9

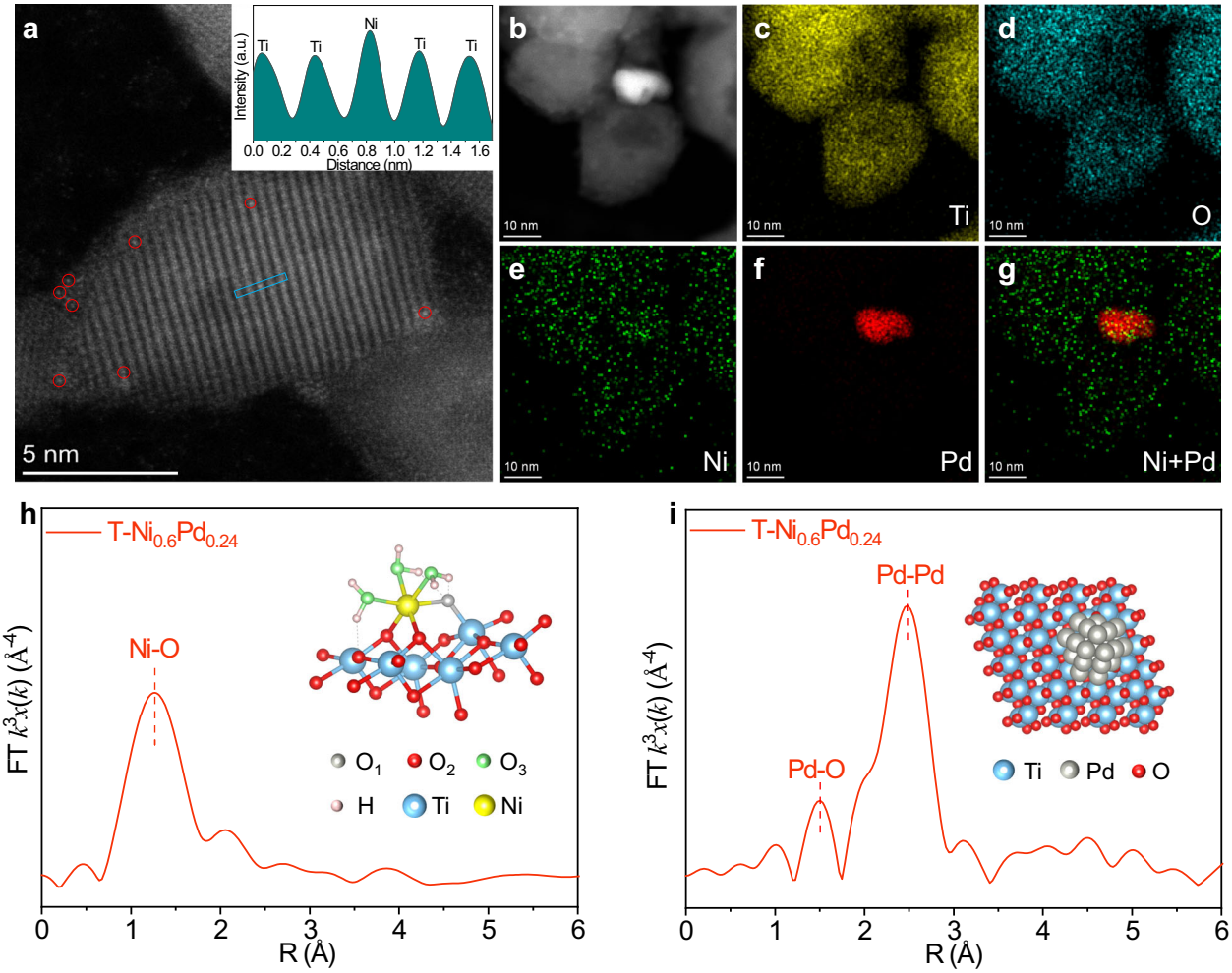

Fig. 2 | Schematic preparation procedure and structural characterizations. **a** HAADF-STEM image of T-$Ni_{0.6}Pd_{0.24}$, where Ni atoms are marked by red circles. The inserted diagram presents the line scan measured along the blue rectangle region marked in (**a**). **b**, **c**, **d**, **e**, **f**, **g**, (**b**–**g**) HAADF and EDX mapping images of T-$Ni_{0.6}Pd_{0.24}$. Yellow, blue, green, and red colors represent Ti (**c**), O (**d**), Ni (**e**), and Pd (**f**) elements, respectively. **h**, k^3-weighted Ni-K-edge EXAFS Fourier transformation spectrum of T-$Ni_{0.6}Pd_{0.24}$ (inset, local geometric structure of isolated Ni atoms grafted on the surface of TiO_2 NPs). The gray ball represents terminal oxygen (O_1), while the red balls represent lattice oxygen (O_2), including surface bridging oxygen. The green ball represents coordinated oxygen in three water molecules (O_3). **i**, k^3-weighted Pd-K-edge EXAFS Fourier transformation spectrum of T-$Ni_{0.6}Pd_{0.24}$ (inset, structural model of Pd NPs photo-deposited on the surface of TiO_2 NPs). Source data are provided with this paper.

field scanning TEM (HAADF-STEM) image of the T-$Ni_{0.6}Pd_{0.24}$ sample shows several isolated bright spots highlighted with red circles on the surface of TiO_2 NPs (Fig. 2a), indicating the formation of atomically isolated Ni sites by the SOMC method. In contrast, Pd is distributed as nanoparticles on the surface of anatase TiO_2 NPs (Fig. 2b), with a measured fringe spacing of 0.22 nm indexed to the (111) plane of Pd (~5 −10 nm) (Supplementary Fig. 7)[30]. The energy-dispersive X-ray spectroscopy (EDS) images reveal that Ti, O, and Ni elements are uniformly distributed on the TiO_2 support, while the Pd element exhibits an aggregated state (Fig. 2b–g). The in situ EPR results confirm the transfer of photogenerated electrons from TiO_2 NPs to isolated Ni sites (Supplementary Fig. 8).

Figure 2h, i show, respectively, the k^3-weighted extended X-ray absorption fine structure (EXAFS) Fourier transformation spectra of Ni and Pd elements in the T-$Ni_{0.6}Pd_{0.24}$ sample. The Fourier transformation Ni K-edge EXAFS data are fitted using a model consisting of a single Ni absorber coordinated to two shells of O atoms (Supplementary Fig. 9) and the Fourier transformation Pd K-edge EXAFS data are fitted by a model consisting of a single Pd absorber coordinated to one shell of O atoms and one shell of Pd atoms (Supplementary Figs. 10–11). The best fit results are given in Supplementary Table 1 and point to the formation of atomically isolated Ni species. Each Ni atom is coordinated, on average, to one terminal O_1 atom of TiO_2 surface with a Ni-O distance of 1.92 Å, two bridging O_2 atoms of TiO_2 surface with a Ni-O distance of 1.98 Å, and to three O_3 atoms of H_2O molecules with a Ni-O distance of 2.23 Å. The local geometric structure of grafted Ni atoms is validated further to be stable by the DFT calculation and is depicted in the inset of Fig. 2h. Each Pd atom is coordinated, on average, to one O atoms with a Pd-O distance of 2.03 Å and to eight Pd atoms with a Pd-Pd distance of 2.74 Å. The Pd-Pd interatomic distance in the T-$Ni_{0.6}Pd_{0.24}$ sample is highly consistent with that (2.73 Å) of Pd bulk, confirming the formation of metallic Pd NPs. The Pd-O interatomic distance is well corresponding to that (2.03 Å) of PdO[24], suggesting that a minor amount of surface Pd atoms of Pd NPs is oxidized to Pd^{2+} by bonding to the surface oxygen atoms of anatase TiO_2 NPs. The X-ray photoelectron spectroscopy (XPS) results further confirm that the oxidation state of Ni is +2 and Pd^0 is predominant in Pd NPs photo-deposited on TiO_2 with a minor amount of Pd^{2+} (Supplementary Fig. 12). The local geometric models of Ni SAs and Pd NPs are depicted, respectively, in the inset of Fig. 2h, i.

https://doi.org/10.1038/s41467-025-64389-9

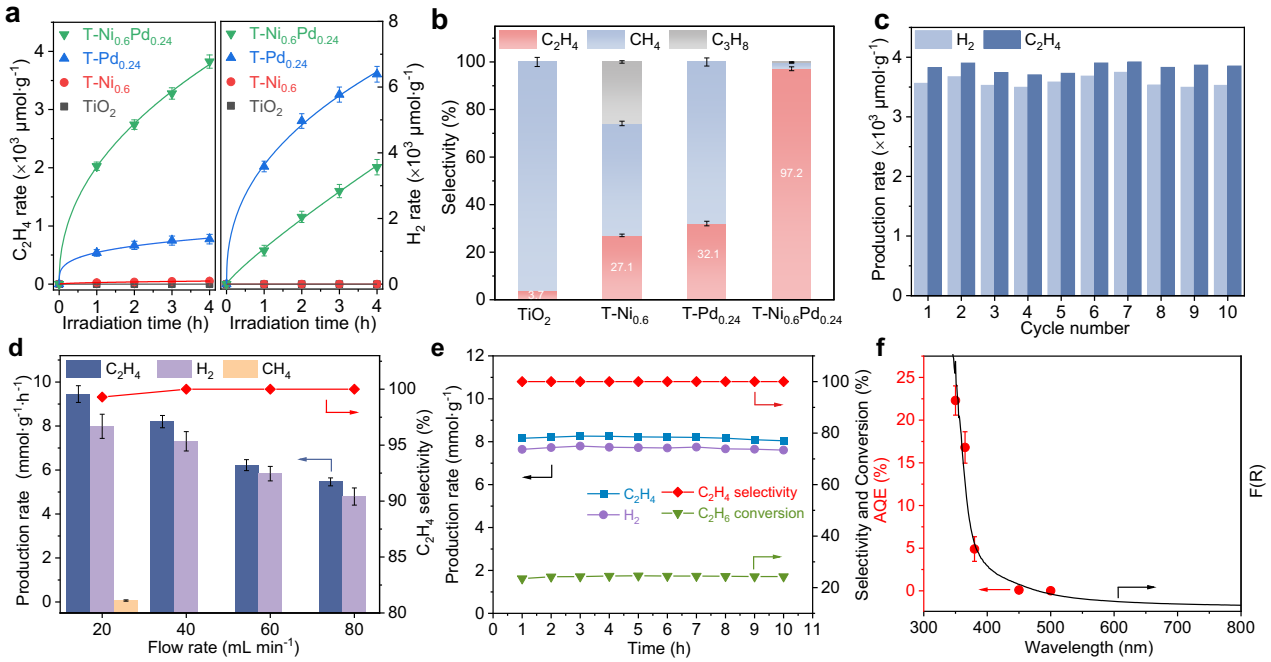

Fig. 3 | Photocatalytic activity and selectivity of photocatalysts under simulated solar light irradiation. a Photocatalytic non-oxidative ethane dehydrogenation activity of the TiO_2, T-$Ni_{0.6}$, T-$Pd_{0.24}$, and T-$Ni_{0.6}Pd_{0.24}$ catalysts in a batch reactor ($n = 5$ independent replicates). **b** Ethene selectivity of all catalysts in a batch reactor ($n = 5$ independent replicates). **c** The photocatalytic cyclic experiment of T-$Ni_{0.6}Pd_{0.24}$ in a batch reactor, with each cycle lasting 4 h. Reaction conditions for **a**–**c**: in a batch reactor with 5 mg of catalysts, C_2H_6: Ar = 1:99, 4 h reaction time, irradiation intensity of 300 mW cm^{-2} (300 W Xe lamp with AM 1.5 G filter). **d** The photocatalytic NOEDH performance of the T-$Ni_{0.6}Pd_{0.24}$ photocatalyst at different total flow rates in a flow reactor ($n = 5$ independent replicates). **e** The stability test of the T-$Ni_{0.6}Pd_{0.24}$ catalyst for 10 h in a flow reactor. **f** Wavelength-depended AQE action spectrum of the T-$Ni_{0.6}Pd_{0.24}$ catalyst ($n = 5$ independent replicates). Reaction conditions for **d**–**f**: in a flow reactor with 5 mg of catalysts, C_2H_6: Ar = 9:91, 10 h reaction time, irradiation intensity of 300 mW cm^{-2} (300 W Xe lamp with AM 1.5 G filter). Source data are provided with this paper.

Simulated solar light-driven photocatalytic activities of non-oxidative EDH

The photocatalytic NOEDH performance of as-synthesized samples is evaluated first in a batch reactor with a feed C2H6: Ar ratio of 1:99. H_2, CH_4, C_2H_4 and C_3H_8 products are detected by gas chromatography, as shown in Supplementary Fig. 13. Figure 3a displays the main products, H_2 and C_2H_4, function with irradiation time under simulated solar light. The parent anatase TiO_2 catalyst exhibits a negligible activity for the NOEDH reaction. CH_4 is the main product with a low production rate of 12.2 μmol·g^{-1}·h^{-1}. No H_2 is evolved within 4 h of irradiation time, while the production rate of C_2H_4 is as low as 0.5 μmol·g^{-1}·h^{-1}, or even negligible. After grafting Ni sites, the production rate of C_2H_4 is increased to 13.7 μmol·g^{-1}·h^{-1}. No H_2 is formed over the T-$Ni_{0.6}$ photocatalyst, whereas a new product, propane, is detected with a rate of 13.1 μmol·g^{-1}·h^{-1}, and its selectivity is almost the same as C_2H_4. The EDH over the T-$Pd_{0.24}$ photocatalyst is boosted significantly. The production rate of C_2H_4 is enhanced to 193.4 μmol·g^{-1}·h^{-1}, whereas the production rate of H_2 is 8.3 times of C_2H_4 and reaches 1597.8 μmol·g^{-1}·h^{-1}. Also, CH_4 is formed at a rate of 410 μmol·g^{-1}·h^{-1}, as a result, the C_2H_4 selectivity is as low as 32.1%, as shown in Fig. 3b. These results indicate the occurrence of C-C bond cleavage and the generation of substantial coke using Pd NPs loaded TiO_2, as further corroborated by post-reaction scanning electron microscopy (SEM) mapping (Supplementary Fig. 14). Interestingly, the C_2H_4 selectivity as high as 97.2% is achieved using the T-$Ni_{0.6}Pd_{0.24}$ photocatalyst at an impressive production rate of 956.3 μmol·g^{-1}·h^{-1} (Fig. 3b). H_2 is produced stoichiometrically at a rate of 890.6 μmol·g^{-1}·h^{-1}, indicating that the grafted Ni SAs enable the stoichiometric conversion of ethane to ethene and H_2 over the surface of Pd NPs. This mechanistic advantage is further supported by post-reaction SEM analysis (Supplementary Fig. 15), which shows only sporadic carbon signals on T-$Ni_{0.6}Pd_{0.24}$ (attributed to ambient adsorption), in stark contrast to the severe coking observed on T-$Pd_{0.24}$. More importantly, the activity stability (Fig. 3c) displays that the T-$Ni_{0.6}Pd_{0.24}$ photocatalyst maintains the high activity and selectivity even after ten cycles. In contrast, the control photocatalyst, T-$Ni_{0.6}$, starts to decrease in C_2H_4 production rate after six cycles (Supplementary Fig. 16). The production rates of H_2 and CH_4 over T-$Pd_{0.24}$ gradually increase within three cycles, indicating the significant coke formation based on the carbon conservation principles. These results demonstrate that the cooperation of Ni single atoms with adjacent Pd NPs efficiently suppresses the deep dehydrogenation and coke formation.

The infrared thermal imaging (FLIR C8940) confirmed that under full spectrum illumination (300 mW·cm^{-2}), the local temperature of the catalyst stabilized at 328 ± 2 K (Supplementary Fig. 17). A series of control experiments conducted without catalysts, C_2H_6, photo-irradiation, and at different temperatures confirmed that the NOEDH reaction is triggered via optical excitation of T-$Ni_{0.6}Pd_{0.24}$ (Supplementary Fig. 18). Even when the reaction was carried out in a dark environment at 673 K, only trace amounts of ethylene were detected, indicating that the contribution of thermally driven catalysis is minimal. Furthermore, the approximate linear relationship between the C_2H_4 yield and irradiation intensity underscores the significant impact of the photo driven effect (Supplementary Fig. 19). When the reaction is performed in the presence of O_2 (Supplementary Fig. 20), the ethene production rate is dramatically decreased to 103.7 μmol·g^{-1}·h^{-1}, while the rates of methane (34.6 μmol·g^{-1}·h^{-1}) and propane (37.0 μmol·g^{-1}·h^{-1}) show a slight increase. It demonstrates that molecular oxygen is an inhibitor for the Pd-catalyzed NODH of ethane to ethene. Compared to Ru and Co (Supplementary Figs. 21–22, and Table 2), Ni is the best promotor for the photocatalytic NOEDH proceeding over the surface of Pd NPs. The reference photocatalyst with NiO and Pd NPs, i-T-

$NiO_{0.6}Pd_{0.24}$, which is prepared using a combined procedure of NiO impregnation with photo-deposition of Pd NPs, gives only a C_2H_4 production rate of 322.8 μmol·g^{-1}·h^{-1} with a selectivity as low as 41% (Supplementary Fig. 23), protruding the superiority of Ni SAs for the NOEDH reaction. The reference photocatalyst prepared by calcination of T-$Ni_{0.6}Pd_{0.24}$ at 400 °C for 12 h, T-$Ni_{0.6}Pd_{0.24}O$, represents a C_2H_4 production rate of 620.7 μmol·g^{-1}·h^{-1} and a 57.7% C_2H_4 selectivity (Supplementary Fig. 24). Both XAFS (Supplementary Figs. 25–26 and Table 3) and XPS characterizations (Supplementary Fig. 27) show that all Pd^0 species are converted in an oxidation state of +2 in the T-$Ni_{0.6}Pd_{0.24}O$ photocatalyst, while the geometric structure and coordination configuration of Ni SAs are not altered. It indicates that metallic Pd NPs are more favorable for the selective cleavage of C-H bonds, compared to PdO NPs. Exceptionally, the T-$Ni_{0.6}Pd_{0.24}$ photocatalyst is also efficient for the photocatalytic NODH of propane to propylene and H_2. A C_3H_6 production rate of 1037.5 μmol·g^{-1}·h^{-1} with 77.2% C_3H_6 selectivity is achieved (Supplementary Figs. 28–32 and Table 4), further confirming that the photocatalytic non-oxidative alkane dehydrogenation is a promising alternative to light alkene production.

Next, we test the photocatalytic performance of T-$Ni_{0.6}Pd_{0.24}$ in a flow reactor with a C_2H_6: Ar ratio of 9: 91. Figure 3d shows the dependence of activity on total flow rate. The C_2H_4 production rate reaches 9.5 mmol·g^{-1}·h^{-1} with 99.3% selectivity when the total flow rate is 20 mL·min^{-1}, with the H_2 production rate of 8.0 mmol·g^{-1}·h^{-1}. As the total flow rate gradually increases to 40, 60, and 80 mL·min^{-1}, the C_2H_4 production rate decreases, respectively, to 8.2, 6.2, and 5.5 mmol·g^{-1}·h^{-1}, accompanied by the stoichiometric hydrogen generation. Surprisingly, the 100% selectivity towards C_2H_4 is obtained for all three tested flow rates (Supplementary Table 5). Under the optimized reaction conditions (at the total flow rate of 40 mL·min^{-1}), a continuous photocatalytic stability test is conducted with the T-$Ni_{0.6}Pd_{0.24}$ photocatalyst for 10 h. No deactivation is discernible, and the C_2H_4 production rate fluctuates around 8.2 mmol·g^{-1}·h^{-1} with 100% C_2H_4 selectivity (Fig. 3e). The XPS curves and XRD spectra indicate that after 10 h of photocatalytic testing, the T-$Ni_{0.6}Pd_{0.24}$ catalyst retained its initial crystal and electronic structure (Supplementary Figs. 33–34). This indicates that the catalyst is photochemically stable for the reaction under anaerobic conditions.

Figure 3f shows the apparent quantum efficiency (AQE) of the optimal T-$Ni_{0.6}Pd_{0.24}$ photocatalyst. It well matches the UV-vis absorption spectrum, where an absorption tail occurs in the visible light region. It originates from the metal-to-metal charge transfer transition (MMCT)[31]. Compared to parent TiO_2, the band edge of T-$Ni_{0.6}Pd_{0.24}$ red-shifts from 385 nm to 410 nm (Supplementary Fig. 35), corresponding to a band gap energy of 3.04 eV (the inset is Tauc plot). As a result, an impressive AQE value of 22.3% is obtained at 350 nm and an AQE value as low as ~0.1% is achieved beyond 410 nm. The results confirm that the EDH is driven by photo-excitation of anatase TiO_2 NPs.

Photocatalytic mechanism and reaction pathways

Figure 4a shows the ^{13}C isotope labeling result of the NOEDH reaction. The strongest ion peak at m/z = 29 is an indicative of $^{13}CH_2 = {}^{12}CH_2$[32], confirming that the reaction is a direct EDH process. The in situ FTIR spectra of the T-$Ni_{0.6}Pd_{0.24}$ catalyst further support this conclusion. As shown in Supplementary Figs. 36–38, vibrational peaks corresponding to C_2 intermediates ($^*C_2H_{4+n}$, $n = 0, 1, 2$) were detected, while no peaks indicative of oxygenated intermediates, such as CH_3CH_2OH (1252 cm^{-1}) were observed. This rules out the participation of lattice oxygen from TiO_2 or H_2O in the reaction. Figure 4b displays the in situ DMPO-trapping EPR spectra of the T-$Pd_{0.24}$ and T-$Ni_{0.6}Pd_{0.24}$ photocatalysts. They are silent in the dark, exposed to C_2H_6 atmosphere, whereas under solar light irradiation, a set of EPR signals belonging to $^{\cdot}C_2H_5$ radical appears besides the set of EPR signals attributed to $^{\cdot}OH$ radical, indicating that C_2H_6 is directly dissociated to $^{\cdot}C_2H_5$ radical and H^+ by photogenerated holes trapped over Pd NPs under light irradiation. Additionally, the DMPO-$^{\cdot}C_2H_5$ signal intensity of the T-$Ni_{0.6}Pd_{0.24}$ photocatalyst is stronger than that of the T-$Pd_{0.24}$ photocatalyst, providing another evidence for achievement of higher charge separation efficiency by the cooperation of isolated Ni sites with Pd NPs, besides the steady-state photoluminescence and transient photocurrent results (Supplementary Figs. 39–40).

DFT calculations are conducted to gain details of the NOEDH reaction pathway. The structural simulation models denoted as T-$Ni_{0.6}$, T-$Pd_{0.24}$, and T-$Ni_{0.6}Pd_{0.24}$, which are corresponding, respectively to the T-$Ni_{0.6}$, T-$Pd_{0.24}$, and T-$Ni_{0.6}Pd_{0.24}$ photocatalysts, are built and optimized based on the characterization results of the above-mentioned XAFS and STEM (Supplementary Fig. 41). On the T-$Ni_{0.6}$ photocatalyst, as shown in Fig. 4c, C_2H_6 is adsorbed on the isolated Ni^{2+} sites with an adsorption energy of +0.02 eV, which is a little higher than those of T-$Pd_{0.24}$ (−0.06 eV) and T-$Ni_{0.6}Pd_{0.24}$ (−0.22 eV). It is disadvantageous for subsequent reactions, i.e., the adsorbed C_2H_6 undergoes the C-H bond dissociation to form $^*C_2H_5$ and $^*H$. This step is thermodynamically favorable and serves as the initial stage in all reaction pathways. The $^*C_2H_5$ conversion follows either a further subtracting hydrogen path or a C-C bond scission. The former produces C_2H_4, whereas the latter is regarded as a channel for coke formation. The C-C bond scission of $^*C_2H_5$ to $^*CH_3$ and $^*CH_2$ adsorbates (−0.08 eV) is more thermodynamically favorable than the further dehydrogenation of $^*C_2H_5$ to $^*C_2H_4$ and $^*H$ (+0.29 eV) (Supplementary Fig. 42). It well explains the CH_4 production. After the product CH_4 molecule is desorbed, a larger energy of +0.17 eV is necessary for the adsorption of another C_2H_6 molecule on the Ni sites due to the presence of $^*CH_2$ adsorbate. Note, the subsequent reaction of $^*C_2H_6 + {}^*CH_2 \rightarrow {}^*C_2H_5 + {}^*CH_3$ proceeds spontaneously (−0.39 eV), along with the spontaneous coupling reaction of $^*C_2H_5 + {}^*CH_3 \rightarrow {}^*C_3H_8$ (Supplementary Fig. 43a-i). The C_3H_8 path is thermodynamically favorable compared to the C_2H_4 path, and thus leads to a decrease in C_2H_4 selectivity.

On the T-$Pd_{0.24}$ photocatalyst, an absolute advantage is occurred in the step of extracting β-H to form $^*C_2H_4$ and 2*H because the reaction energy barrier of −0.34 eV is far lower than those of T-$Ni_{0.6}$ (+0.85 eV) and T-$Ni_{0.6}Pd_{0.24}$ (+0.45 eV) (Fig. 4c). The low desorption energy (−0.04 eV) is advantageous for the generation of H_2 in terms of kinetics, while the high desorption energy, as large as +1.25 eV for C_2H_4 desorption, poses a fatal blocking point towards realizing efficient C_2H_4 production. The potential energy diagram shows two coke formation pathways. One is the further dehydrogenation of $^*C_2H_4$ to $^*C_2H_3$ and $^*H$, ultimately leading to excessive production of H_2 and coke formation because C_2H_4 is difficult to desorb on the surface of Pd NPs (Supplementary Figs. 44–45). The path is thermodynamically prohibited due to the large energy barrier of +3.0 eV. Another is the C-C cleavage path, where $^*C_2H_5$ is cracked to $^*CH_3$ and $^*CH_2$, and then proceeds the deep dehydrogenation to form coke and H_2. It is a thermodynamically-permitted process. The negative energy barrier of −0.30 eV indicates that the formation of H_2 and coke formation by the C-C dissociation of $^*C_2H_5$ ($C_2H_6 \rightarrow C + H_2$) is preferred to the C_2H_4 production over the surface of Pd NPs. It is highly consistent with its photocatalytic performance, as the ratio of H_2 to C_2H_4 is much greater than the stoichiometric ratio of 1:1.

Introducing Ni SAs modifies the pathway of NOEDH reaction over adjacent Pd NPs. As shown in Fig. 4c, on the T-$Ni_{0.6}Pd_{0.24}$ photocatalyst, the C_2H_6 adsorption capacity is enhanced, and the desorption of C_2H_4 product from the surface of Pd NPs is promoted. The desorption energy significantly decreases from +1.25 to +0.21 eV. The C_2H_4 temperature-programmed desorption (TPD) further validated the afore-mentioned conclusions (Supplementary Fig. 46). Compared to T-$Pd_{0.24}$ (desorption peaks at 296 C/388 °C), the desorption peaks of Ni SA modified T-$Ni_{0.6}Pd_{0.24}$ shifted significantly to lower temperatures

https://doi.org/10.1038/s41467-025-64389-9

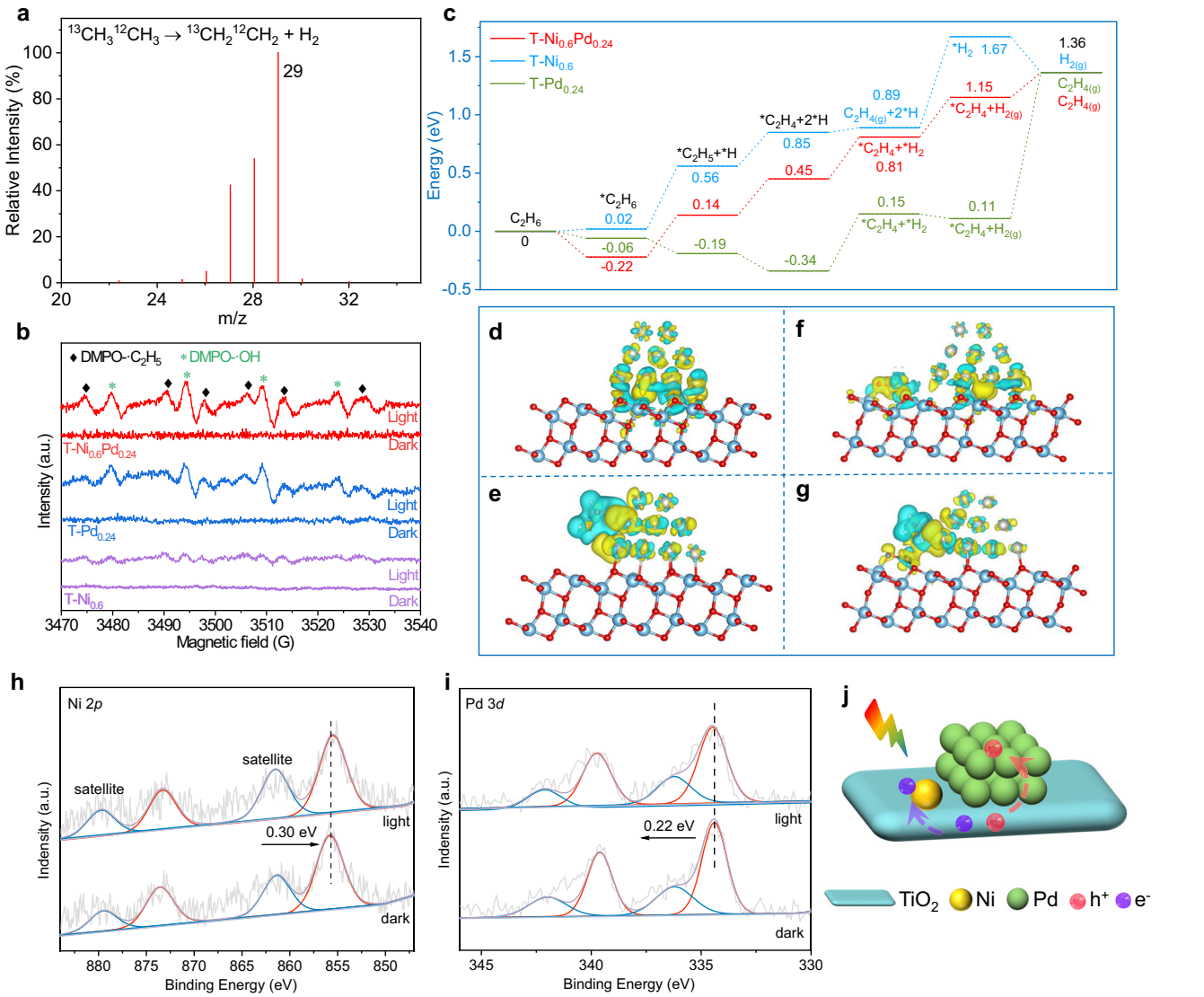

Fig. 4 | Photocatalytic mechanism and reaction pathway. a The $^{13}CH_3{}^{12}CH_3$ isotope labeling result: Mass spectrum of the dehydrogenation product C_2H_4. **b** In situ DMPO-trapping EPR spectra of T-$Ni_{0.6}$, T-$Pd_{0.24}$, and T-$Ni_{0.6}Pd_{0.24}$ photocatalysts exposed to C_2H_6 atmosphere in dark and under solar light irradiation. **c** Reaction energy diagrams for the conversion of C_2H_6 to C_2H_4 over the T-$Ni_{0.6}$, T-$Pd_{0.24}$, and T-$Ni_{0.6}Pd_{0.24}$ catalysts. **d** The differential charge density profile of the T- $Pd_{0.24}$ photocatalyst. **e** The differential charge density profile of the T-$Pd_{0.24}$ photocatalyst with adsorbed C_2H_6. **f** The differential charge density profile of the T-$Ni_{0.6}Pd_{0.24}$ photocatalyst. **g** The differential charge density profile of the T-$Ni_{0.6}Pd_{0.24}$ photocatalyst with adsorbed C_2H_6. Yellow and cyan regions correspond, respectively, to electron density gain (accumulation) and loss (depletion). **h**,**i** In situ XPS spectra of T-$Ni_{0.6}Pd_{0.24}$ (Ni 2*p*, Pd 3 *d*) under dark and light irradiation conditions. **j** Schematic illustration of the charge transfer mechanism in T-$Ni_{0.6}Pd_{0.24}$. Source data are provided with this paper.

(198 °C/275 °C) with reduced peak areas, confirming that the incorporation of Ni SAs weakens the ethylene adsorption strength and reduces the adsorption capacity on the Pd surface. Notably, the T-$Ni_{0.6}Pd_{0.24}$ catalyst exhibits a significantly lower activation energy for the cleavage of the first C-H bond in ethane, outperforming both T-$Ni_{0.6}$ and T-$Pd_{0.24}$ (Supplementary Fig. 47). After the second dehydrogenation, the formed $*C_2H_4$ adsorbate does not undergo the deep dehydrogenation because there is a high H_2 formation energy barrier of +0.78 V on the Ni sites (Supplementary Figs. 48–49). As a result, a considerable C_2H_4 yield with high selectivity is achieved over the T-$Ni_{0.6}Pd_{0.24}$ photocatalyst. More notably, the dehydrogenation energy of $*C_2H_5$ to $*C_2H_4$ increases from −0.34 to +0.45 eV, but the C-C cleavage energy increases dramatically from +0.11 to +1.49 eV (Supplementary Figs. 50-51), implying that the grafted Ni SAs make the C-C cleavage path proceeding on Pd NPs unfavorable. It explains well the coke resistance of the T-$Ni_{0.6}Pd_{0.24}$ photocatalyst. The number of Ni SAs adjacent to Pd NPs does not affect the thermodynamics of the reaction. The DFT calculation results indicate that with increasing Ni SAs adjacent to Pd NPs, no remarkable difference in energy barrier of elemental reaction steps is observed for T-Ni_1Pd, T-Ni_2Pd, and T-Ni_3Pd (Supplementary Figs. 52–56).

Finally, it appears from Fig. 4d representing the differential charge density profile that the charge density of Pd atoms at the Pd/TiO_2 interface is significantly larger than that of surface Pd atoms exposed to the reactant due to the metal-semiconductor interaction. Upon adsorption of C_2H_6 on the bare Pd atoms (Fig. 4e), the charges accumulated initially at the Pd/TiO_2 interface are completely depleted and transferred to the C_2H_6-Pd region, forming the highly electron-deficient $*C_2H_6$ adsorbate. The close proximity of Ni SAs to Pd NPs leads to a significant change in charge density distribution (Fig. 4f). The charges are accumulated at the Ni atom, and yet the charge density of Pd atoms in Pd NPs is highly depleted, especially for those neighboring

the Ni atom. On the T-$Ni_{0.6}Pd_{0.24}$ photocatalyst, C_2H_6 is preferentially adsorbed on the Ni and adjacent Pd atoms (Fig. 4g), where the charges are accumulated at the adsorbate-metal region. Overall, grafting of Ni SAs modulates the surface electronic structure of adjacent Pd NPs, allowing thermodynamically and kinetically the selective dehydrogenation of C_2H_6 to C_2H_4 and H_2. To further verify the conclusion, the charge transfer behaviors of T-$Ni_{0.6}$, T-$Pd_{0.24}$, and T-$Ni_{0.6}Pd_{0.24}$ catalysts under light irradiation were observed using in situ XPS. As shown in Supplementary Fig. 57, when the reference sample T-$Ni_{0.6}$ is irradiated by light, a slight shift of *ca*. 0.24 eV towards low binding energy is discernible on the Ni 2*p* XPS spectra, while the Ti 2*p* and O 1*s* binding energies are shifted towards high binding energy by 0.15 eV and 0.20 eV, respectively. These results further indicate that photogenerated electrons are transferred to the grafted Ni species through the Ti-O-Ni linkage. Supplementary Fig. 58 show that the photo-irradiation of the T-$Pd_{0.24}$ reference catalyst makes the Pd 3*d* XPS peaks shifted by 0.18 eV towards high binding energy, confirming that Pd acts as a hole acceptor. As expected, after photo-irradiation of the T-$Ni_{0.6}Pd_{0.24}$ photocatalyst, the Ni 2*p* binding energy is shifted by −0.30 eV, along with a +0.22 eV shift of the Pd 3*d* binding energy, as shown in Fig. 4h, i and Supplementary Fig. 59. This result provides another solid evidence for the conclusion that photogenerated electrons are transferred from TiO_2 to Ni SAs and holes are transferred to Pd NPs upon photoexcitation of the T-$Ni_{0.6}Pd_{0.24}$ catalyst (Fig. 4j). Therefore, the pathway of photocatalytic NOEDH reaction proceeding over T-$Ni_{0.6}Pd_{0.24}$ is depicted clearly in Fig. 1. C_2H_6 is adsorbed initially on the Ni-Pd pair. Upon solar light irradiation, the photo-generated holes and electrons transfer from photoexcited TiO_2 NPs to Pd NPs and Ni SAs, respectively. The holes trapped on the surface of Pd NPs oxidize the C-H bond of C_2H_6 adsorbates to form ethyl radical ($^{\bullet}C_2H_5$) and H^+ ($^{\bullet}C_2H_5$ is adsorbed on Pd sites and H^+ is adsorbed on Ni sites). Subsequently, a β-H atom of $^{\bullet}C_2H_5$ radical is extracted by the hole oxidation to generate C_2H_4. H^+ is finally reduced to H_2 by electrons trapped on Ni sites.

In summary, the findings presented here mark progress in the solar ethene production by a Ni-modified non-oxidative EDH pathway. Grafting of Ni SAs on the surface of anatase TiO_2 NPs to twin with photo-deposited Pd NPs enables the efficient photocatalytic NODH of ethane to ethene and H_2. A high rate of 8.2 $mmol \cdot g^{-1} \cdot h^{-1}$ is achieved in a flow reactor under solar light irradiation, and an AQE of ~22.3% is obtained at 350 nm. The C_2H_4 selectivity reaches 100% at a reactant flow rate of ≥ 40 $mL \cdot min^{-1}$. No coke formation and no deactivation are observed after 10 h of photocatalytic reaction in the flow reactor, indicating that the as-synthesized T-$Ni_{0.6}Pd_{0.24}$ photocatalyst is highly stable for the NOEDH reaction. The product ratio of C_2H_4 to H_2 is approximate to a stoichiometric proportion, demonstrating the perspective of significant economic incentives. This work opens a window for the large-scale and high-rate solar alkene production by a non-oxidative alkane dehydrogenation route.

Methods

Chemicals

Anatase TiO_2 (Alfa Aesar, 99.7%, 20 nm, 82.0 $m^2 \cdot g^{-1}$) underwent purification by calcination at 673 K under oxygen flow for 12 h to remove surface organic adsorbates, prior to catalyst synthesis. Nickelocene ($(C_5H_5)_2Ni$, $(Cp)_2Ni$, 98%), ruthenocene ($(C_5H_5)_2Ru$, $(Cp)_2Ru$, 98%), cobaltocene ($(C_5H_5)_2Co$, $(Cp)_2Co$, 98%), n-hexane (n-C_6H_{14}), and palladium (II) chloride ($PdCl_2$, 99%) were purchased from Aladdin. Hydrochloric acid (HCl, 36.5 − 38.0 wt%) was supplied by Sinopharm Chemical Reagent Beijing Co., Ltd. All of the above chemicals were used without further purification.

Preparation of catalysts

Preparation of T-Ni_x photocatalysts. The TiO_2-Ni catalyst (denoted as T-Ni_x) was prepared via surface organometallic chemistry[28]. Synthesis involved a vacuum-connected glass apparatus, where 50 mg of anatase TiO_2 was initially calcined at 673 K under oxygen flow for 12 h to eliminate surface organic adsorbates, followed by dynamic vacuum treatment (10^{-2} Pa) at the same temperature for 3 h to remove adsorbed moisture. After cooling to ambient conditions, 100 µL of nickelocene solution (5 mg/mL in n-hexane) was introduced into the reactor via syringe and allowed to react with TiO_2 at 403 K for 30 h. To mitigate nickelocene oxidation, the injection was performed within an inert glovebox environment. Prior to the reaction, residual n-hexane was largely evacuated through a brief 3 min vacuum step. Post-reaction, unreacted nickelocene residues were stripped from the TiO_2 surface by reapplying dynamic vacuum at 403 K for 3 h. The resulting material was subsequently subjected to final calcination at 673 K for 12 h to yield T-Ni_x.

Preparation of T-Ru photocatalysts. The process was the same as that for the preparation of T-Ni_x, but the nickelocene in the original process was changed to ruthenocene, and the reaction condition was 30 h at 423 K.

Preparation of T-Co photocatalysts. The steps and reaction conditions for preparing T-Ni_x were the same, and the nickelocene in the original process was changed to cobaltocene.

Preparation of T-Pd_y photocatalysts. T-Pd catalyst was prepared by the photochemical reduction method[26]. In a typical experiment, for example, 30 mg of anatase TiO_2 was dispersed in 50 ml of deionized water. H_2PdCl_4 solution was prepared by dissolving $PdCl_2$ (50 mg) in 1 M HCl (50 mL) aqueous solution. Subsequently, 0.7 mL of this solution was added to a TiO_2 suspension. The mixture was irradiated with a 300 W xenon lamp for 5 min. After that, the sample was washed with deionized water at least three times and dried at 80 °C overnight to produce the sample.

Preparation of T-$Ni_{0.6}Pd_{0.24}$ photocatalysts. The preparation method was the same as the preparation of T-Pd_y, and the raw material TiO_2 was replaced by T-Ni_x.

Preparation of T-$Ni_{0.6}Pd_{0.24}O$ photocatalysts. The sample T-$Ni_{0.6}Pd_{0.24}$ was calcined in 400 °C air for 12 h.

Preparation of T-RuPd0.24 photocatalysts. The preparation method was the same as the preparation of T-Pd_y, and the raw material TiO_2 was replaced by T-Ru.

Preparation of T-CoPd0.24 photocatalysts. The preparation method was the same as the preparation of T-Pd_y, and the raw material TiO_2 was replaced by T-Co.

Preparation of i-T-NiO.6 photocatalysts. The i-T-$Ni_{0.6}$ was prepared using the impregnation method, with the same Ni content as T-Ni_x.

Preparation of i-T-NiO.6PdO.24 photocatalysts. The preparation method was the same as the preparation of T-Pd_y, and the raw material TiO_2 was replaced by i-T-$Ni_{0.6}$.

Calculation methods. The DFT calculations were performed on the Vienna Ab initio Simulation Package (VASP) code[33,34]. The interaction of core and electrons was treated by projector augmented wave (PAW) pseudopotential[35,36] with a cut-off energy of 550 eV. The exchange-correlation function was described by the generalized-gradient approximation-Perdew-Burke-Ernzerhof (GGA-PBE)[37]. The DFT-D3(BJ) method was used to consider the van der Waals (vdW) dispersion energy correction[38]. Convergence in geometry optimization was reached when the force on each atom fell below 0.02 eV $Å^{-1}$. A vacuum

layer of 16 Å was introduced to eliminate the interaction between two adjacent slabs. The Brillouin zone sampling was performed using Gamma-centered Monkhorst-Pack (MP) grids[39], and the k-point was set as 3×3×1 for all the DFT calculations. The data processing was assisted by VASPKIT[40], QVASP[41] and VESTA[42] software. The Gibbs free energy difference (ΔG) between initial and final states was denoted as:

$$\Delta G = \Delta E + \Delta ZPE - T\Delta S \quad (1)$$

where E, ZPE, T, and S represent the energy from DFT calculation, zero-point energy, temperature (328.15 K), and entropy, respectively[43,44]. The atomic coordinates of all DFT-optimized structures are provided in the Source Data file (Supplementary Data 1).

Photocatalytic activity measurements. Photocatalytic EDH was conducted in a customized glass-closed batch reactor (190 mL in volume) equipped with a quartz window on top to harvest light irradiation. Typically, 5 mg of catalyst was dispersed into 1 mL of H_2O and sonicated for 5 min to get a slurry, which was then coated on a quartz disk and dried to form a catalyst film. Afterward, the obtained catalyst film was fixed in the reactor, all experiments were performed under an atmosphere pressure (101 kPa). Before the reaction, the system was evacuated by a mechanical pump and then filled with 101 kPa of high-purity Ar (>99.99%) for 30 min to completely remove O_2 from the system. Subsequently, 2 mL of C_2H_6 was injected into the system with a syringe. Then, the system was irradiated under a 300 W Xe lamp (300 mW/cm^2, PerfectLight, PLS-SXE300D) equipped with an AM 1.5 G filter at a constant stirring speed of 500 r/min at room temperature, and the irradiance of the Xe lamp was measured by a light intensity meter (ILT950). Finally, 0.5 mL gas was taken out every 1 h and injected into gas chromatography (GC) to detect the concentration of products. The resulting alkanes were analyzed by gas chromatography with a flame ionization detector (FID) on an Agilent 7890 A, and the gaseous product was separated by an HP-PLOT Q capillary column. The hydrogen was analyzed by GC with thermal conductivity detector (TCD) on an Agilent 7890B, and the product gas was separated by 5 A molecular sieve-packed column and Porapak Q-packed column. Ar was used as carrier gas of the GC. For stability tests, the catalyst-coated quartz disk was subjected to ten consecutive 4 h reaction cycles in the batch reactor. After each cycle, the reactor was evacuated and purged with Ar for 30 minutes to remove residual gases, followed by injection of fresh C_2H_6 (2 mL) for the next cycle. The catalyst was not washed or treated between cycles.

The photocatalytic NOEDH test was conducted in a fixed bed flow reactor with quartz windows at the top, which had a volume of 40 mL. Typically, 5 mg of photocatalyst was dispersed in 1 ml of H_2O by ultrasonication and uniformly coated onto a glass fiber membrane, which was then placed in the flow reactor after drying. A mixture of 9% C_2H_6 and 91% Ar gas was introduced into the reactor at total flow rates of 20, 40, 60, and 80 mL/min, respectively. After purging for one hour under dark conditions to remove air, irradiation was carried out using a 300 W Xe lamp at room temperature with an intensity of 300 mW/cm^2.

The reactant conversion and the selectivity of the products were calculated according to the equation in the following.

$$\text{Conversion}(\%) = \frac{[\text{ethane}]\text{inlet} - [\text{ethane}]\text{oulet}}{[\text{ethane}]\text{inlet}} \times 100\% \quad (2)$$

$$\text{Selectivity}(\%) = \frac{[\text{ethene}]}{[\text{ethene}] + [\text{methane}] + [\text{propane}]} \times 100\% \quad (3)$$

$$\text{Carbonbalance}(\%) = \frac{\text{Molesofproductsintermsofcarbon}}{\text{Molesofethaneconsumed}} \times 100\% \quad (4)$$

The carbon balance for T-$Ni_{0.6}Pd_{0.24}$ is 93.8%, while that for T-$Pd_{0.24}$ is only 34.3%.

Apparent quantum efficiency (AQE)

$$\text{AQE} = \frac{\text{qe}}{\text{qp}} \times 100\% \quad (5)$$

$$qe = \frac{2n(C_2H_4)}{vm \times 3600 \times 10^6} \quad (6)$$

$$qp = \frac{P \times \lambda \times S}{h \times c \times NA} \quad (7)$$

where q_e is the total molar number of electrons transferred in the reaction. $n(C_2H_4)$ represents the yield of produced C_2H_4. The $n(C_2H_4)$ at 350 nm is 732 μL·h^{-1}. The $n(C_2H_4)$ at 365 nm is 613.5 μL·h^{-1}. The $n(C_2H_4)$ at 380 nm is 238 μL·h^{-1}. The $n(C_2H_4)$ at 450 and 500 nm is 0. 3600 (seconds, the conversion factor from hours to seconds). v_m is 22.4 L·mol^{-1}.q_p is the photon flux (number of photons per second), P is the power of the light (W·cm^{-2}), S is 4.9 cm^{-2}, λ is the wavelength (nm), h is Planck's constant (6.626×10^{-34} J·s^{-1}), c is the speed of light (3×10^8 m·s^{-1}) and N_A is the Avogadro's constant (6.02×10^{23} mol^{-1}). The light power P at different wavelengths (λ = 350, 365, 380, 450, and 500 nm) was measured to be 5.68, 6.06, 7.74, 19.2, and 18.9 mW cm^{-2} by xenon lamp (300 W Xe lamp) source and band pass filter. Power and wavelength of the light were measured by a light intensity meter (ILT950). Relevant example calculations are provided in the Supporting Information.

Catalyst characterizations. The XRD measurements were conducted on a Bruker D8 Advance X-ray diffractometer with Cu $K_{\alpha 1}$ radiation (λ = 1.5406 Å) in a scan range of 20 − 80°. The accelerating voltage and the applied current were 40 kV and 40 mA, respectively. The ultraviolet-visible diffuse reflectance (UV-vis DRS) spectra were collected on a Varian Cary 500 Scan UV-vis-NIR spectrometer with Ba_2SO_4 as a reference in a range of 200–800 nm. The X-ray photoelectron spectroscopy (XPS) spectra were carried out on a VG ESCALAB 250 XPS System with a monochromatized Al Kα X-ray source (15 kV, 200 W, 500 μm). All binding energies were calibrated with the C1*s* peak at 284.6 eV of surface adventitious carbon. In situ XPS test conditions: the in situ XPS measurements were performed using a 300 W xenon lamp as the light source (wavelength range of 320 − 800 nm). Reflective and transmissive infrared filters were employed to eliminate thermal effects, with the optical fiber output power ranging from 15 to 30 mW. At a spot diameter of 5 mm, the light power density was measured to be 76.4 − 153 mW/cm^2, which closely approximates the conditions of solar radiation at the Earth's surface. The EPR spectrum was recorded by a Bruker A-300-EPR spectrometer, the test was carried out in a homemade in situ EPR. DMPO··C_2H_5 and DMPO··OH trapping experiment conditions: 3 mg of catalyst was dispersed in 2 mL of deionized water. After adding 20 μL of DMPO and mixing homogeneously, a small amount of the mixture was transferred into a homemade in-situ EPR tube. Subsequently, 2 mL of C_2H_6 gas was introduced under vacuum, and tests were performed in the dark and under irradiation (using the same xenon lamp as in performance testing). Low-temperature EPR tests were conducted at liquid nitrogen temperature using 10 mg of sample, which was degassed at 473 K to remove trace surface-adsorbed gases and other substances. Then, in a vacuum, 2 mL of C_2H_6 gas was introduced, and tests were carried out in the dark and under irradiation. In situ FTIR measurements were carried out using a custom infrared reaction cell coupled to a vacuum line. Following a procedure similar to that reported in previous studies[29,45], the catalyst powder was compressed into a self-supported wafer (18 mm in diameter, ca. 25–30 mg in weight) and mounted onto a movable

holder inside the quartz IR tube. Prior to spectral acquisition, the sample was degassed to eliminate any adsorbed species and impurities. All IR spectra were collected on a Nicolet iS 50 FTIR instrument configured with a DTGS detector, employing a spectral resolution of 4 cm^{-1} and accumulating 32 scans per spectrum. The morphology and composition of the samples were obtained by SEM equipped with energy spectrum (Thermo Scientific Apreo, USA).

X-ray absorption fine structure (XAFS) spectra at the Ni and Pd K-edges were acquired at the BL14W beamline of the Shanghai Synchrotron Radiation Facility (SSRF), operating at 3.5 GeV and 200 mA. A Si (111) double-crystal monochromator was used for energy selection, and the data were collected in fluorescence mode with a Lytle detector under ambient conditions, in accordance with established practices[46,47]. For background subtraction and X-ray absorption near-edge structure (XANES) normalization, a linear polynomial was fitted to the pre-edge region and a third-order polynomial to the post-edge region[47]. To obtain the interatomic distances (R), structural parameters, phase shifts, and backscattering amplitudes extracted from reference Ni or Pd metal were used to fit the EXAFS data. Sub-angstrom-resolution high-angle annular dark-field scanning transmission electron microscopy (HAADF-STEM) characterization was conducted on a Titan Themis G2 300 with a guaranteed resolution of 0.06 nm. Photoluminescence (PL) profiles were performed on Hitachi Fluorescence Spectrophotometer F-7000 with a 350 nm laser excitation source. Photoelectrochemical (PEC) measurements were performed using a conventional three-electrode electrochemical cell with a platinum foil counter electrode, a working electrode, and a saturated Ag/AgCl electrode as a reference electrode. Inductively Coupled Plasma (ICP) was performed on the PerkinElmer Avio 200 catalyst characterization system.

Data availability

The data that support the findings of this study are all available within the paper and its Supplementary Information. Source data are available for Figs. 1h-i, 2a-f, 3a-c, h-i, and Supplementary Figs. 2, 3, 6–13, 16, 18–40, 42, 44, 46–48, 50, 53, and 57–59 in the source data file. Source data are provided with this paper.

References

1. Rahman, M. Z. The dawn of solar ethene. *Nat. Rev. Chem.* **8**, 568 (2024).
2. Zhong, L. et al. Cobalt carbide nanoprisms for direct production of lower olefins from syngas. *Nature* **538**, 84–87 (2016).
3. Song, R. et al. Ethene production via photocatalytic dehydrogenation of ethane using $LaMn_{1-x}Cu_xO_3$. *Nat. Energy* **9**, 750–760 (2024).
4. Zhang, B. et al. Highly electrocatalytic ethene production from CO_2 on nanodefective Cu nanosheets. *J. Am. Chem. Soc.* **142**, 13606–13613 (2020).
5. Thomas, M. et al. Deliberating the perceived risks, benefits, and societal implications of shale gas and oil extraction by hydraulic fracturing in the US and UK. *Nat. Energy* **2**, 1–7 (2017).
6. Mayfield, E. N. et al. Cumulative environmental and employment impacts of the shale gas boom. *Nat. Sustain.* **2**, 1122–1131 (2019).
7. Zhang, H. et al. Activation of light alkanes at room temperature and ambient pressure. *Nat. Catal.* **6**, 666–675 (2023).
8. Hu, Z. et al. High-rate and selective C_2H_6-to-C_2H_4 photodehydrogenation enabled by partially oxidized $Pd^{\delta+}$ species anchored on ZnO nanosheets under mild conditions. *J. Am. Chem. Soc.* **146**, 16490–16498 (2024).
9. Yang, Z. et al. Coking-resistant iron catalyst in ethane dehydrogenation achieved through siliceous zeolite modulation. *J. Am. Chem. Soc.* **142**, 16429–16436 (2020).
10. Najari, S. et al. Oxidative dehydrogenation of ethane: catalytic and mechanistic aspects and future trends. *Chem. Soc. Rev.* **50**, 4564–4605 (2021).
11. Jin, R. et al. Low temperature oxidation of ethane to oxygenates by oxygen over iridium-cluster catalysts. *J. Am. Chem. Soc.* **141**, 18921–18925 (2019).
12. Nakaya, Y. et al. Single-atom Pt in intermetallics as an ultrastable and selective catalyst for propane dehydrogenation. *Nat. Commun.* **11**, 2838 (2020).
13. Phadke, N. M., Mansoor, E., Bondil, M., Head-Gordon, M. & Bell, A. T. Mechanism and kinetics of propane dehydrogenation and cracking over Ga/H-MFI prepared via vapor-phase exchange of H-MFI with $GaCl_3$. *J. Am. Chem. Soc.* **141**, 1614–1627 (2018).
14. Searles, K. et al. Highly productive propane dehydrogenation catalyst using silica-supported Ga-Pt nanoparticles generated from single-sites. *J. Am. Chem. Soc.* **140**, 11674–11679 (2018).
15. Ryoo, R. et al. Rare-earth-platinum alloy nanoparticles in mesoporous zeolite for catalysis. *Nature* **585**, 221–224 (2020).
16. Zhao, D. et al. In situ formation of ZnO_x species for efficient propane dehydrogenation. *Nature* **599**, 234–238 (2021).
17. Motagamwala, A. H. et al. Stable and selective catalysts for propane dehydrogenation operating at thermodynamic limit. *Science* **373**, 217–222 (2021).
18. Wang, P. et al. Photocatalytic ethene production by oxidative dehydrogenation of ethane with dioxygen on ZnO-supported PdZn intermetallic nanoparticles. *Nat. Commun.* **15**, 789 (2024).
19. Li, X. et al. Enhanced stability of Pt/Al_2O_3 modified by Zn promoter for catalytic dehydrogenation of ethane. *J. Energy Chem.* **51**, 14–20 (2020).
20. De, S. et al. Stable Cr-MFI catalysts for the nonoxidative dehydrogenation of ethane: catalytic performance and nature of the active sites. *ACS Catal.* **11**, 3988–3995 (2021).
21. Zhang, L. et al. Visible-light-driven non-oxidative dehydrogenation of alkanes at ambient conditions. *Nat. Energy* **7**, 1042–1051 (2022).
22. Brencio, C. et al. Kinetic model for Pd-based membranes coking/deactivation in propane dehydrogenation processes. *Chem. Eng. J.* **452**, 139125 (2023).
23. Peters, T. A. et al. Investigation of Pd-based membranes in propane dehydrogenation (PDH) processes. *Chem. Eng. J.* **305**, 191–200 (2016).
24. Singh, S. P., Yamamoto, A. & Yoshida, H. Nonoxidative coupling of ethane with gold loaded photocatalysts. *Catal. Sci. Technol.* **12**, 1551–1561 (2022).
25. Li, Q. et al. A photocatalytic transformation realized by Pd/TiO_2 particle size modulation: from oxidative dehydrogenation of ethane to direct dehydrogenation of ethane. *Chem. Eng. J.* **395**, 125120 (2020).
26. Zhang, R. et al. Photocatalytic oxidative dehydrogenation of ethane using CO_2 as a soft oxidant over Pd/TiO_2 catalysts to C_2H_4 and syngas. *ACS Catal.* **8**, 9280–9286 (2018).
27. Song, X. et al. Single-atom Ni-modified Al_2O_3-supported Pd for mild-temperature semi-hydrogenation of alkynes. *ACS Catal.* **12**, 14846–14855 (2022).
28. Zhang, P. et al. Single-site Ni-grafted TiO_2 with diverse coordination environments for visible-light hydrogen production. *ChemSusChem* **17**, e202301041 (2023).
29. Fan, L. et al. Single-site nickel-grafted anatase TiO_2 for hydrogen production: toward understanding the nature of visible-light photocatalysis. *J. Catal.* **320**, 147–159 (2014).
30. Gao, R. et al. Pd/Fe_2O_3 with electronic coupling single-site Pd-Fe pair sites for low-temperature semihydrogenation of alkynes. *J. Am. Chem. Soc.* **144**, 573–581 (2021).
31. Jiao, C. Q. et al. Effect of intermolecular interactions on metal-to-metal charge transfer: a combined experimental and theoretical investigation. *Angew. Chem. Int. Ed.* **131**, 17165–17171 (2019).
32. Gao, Y. et al. Revealing the lattice carbonate mediated mechanism in $Cu_2(OH)_2CO_3$ for electrocatalytic reduction of CO_2 to C_2H_4. *Sci. Adv.* **11**, 2308949 (2024).

33. Kresse, G. & Furthmüller, J. Efficiency of ab-initio total energy calculations for metals and semiconductors using a plane-wave basis set. *Comput. Phys. Commun.* **6**, 15–50 (1996).
34. Kresse, G. & Furthmüller, J. Efficient iterative schemes for ab initio total-energy calculations using a plane wave basis set. *Phys. Rev. B.* **54**, 11169–11186 (1996).
35. Kresse, G. & Joubert, D. From ultrasoft pseudopotentials to the projector augmented-wave method. *Phys. Rev. B.* **59**, 1758–1775 (1999).
36. Blöchl, P. E. Projector augmented-wave method. *Phys. Rev. B.* **50**, 17953–17979 (1994).
37. Perdew, J. P., Burke, K. & Ernzerhof, M. Generalized gradient approximation made simple. *Phys. Rev. Lett.* **77**, 3865–3868 (1996).
38. Grimme, S., Ehrlich, S. & Goerigk, L. Effect of the damping function in dispersion corrected density functional theory. *J. Comput. Chem.* **32**, 1456–1465 (2011).
39. Chadi, D. J. & Cohen, M. L. Special points in the Brillouin zone. *Phys. Rev. B.* **8**, 5747–5753 (1973).
40. Wang, V., Xu, N., Liu, J. C., Tang, G., Geng, W. & Vaspkit, T. A user-friendly interface facilitating high-throughput computing and analysis using VASP code. *Comput. Phys. Commun.* **267**, 108033 (2021).
41. Yi, W., Tang, G., Chen, X., Yang, B. & Liu, X. QVASP: A flexible toolkit for VASP users in materials simulations. *Comput. Phys. Commun.* **257**, 107535 (2020).
42. Momma, K. & Izumi, F. VESTA 3 for three-dimensional visualization of crystal, volumetric and morphology data. *J. Appl. Crystallogr.* **44**, 1272–1276 (2011).
43. Nørskov, J. K. et al. Origin of the overpotential for oxygen reduction at a fuel-cell cathode. *J. Phys. Chem. B.* **108**, 17886–17892 (2004).
44. Zhang, J. et al. Strong metal-support interaction boosts activity, selectivity, and stability in electrosynthesis of H_2O_2. *J. Am. Chem. Soc.* **144**, 2255–2263 (2022).
45. Zhang, P. et al. Surface Ru-H bipyridine complexes-grafted TiO_2 nanohybrids for efficient photocatalytic CO_2 methanation. *J. Am. Chem. Soc.* **145**, 5769–5777 (2023).
46. Liu, H. et al. Nanolayered bismuth oxyselenide for field-effect transistors and photodetectors. *ACS Appl. Nano Mater.* **8**, 4100–4108 (2025).
47. Zhang, P. et al. Platinum single-atom nests boost solar-driven photocatalytic non-oxidative coupling of methane to ethane. *J. Am. Chem. Soc.* **146**, 24150–24157 (2024).

Acknowledgements

This work is supported by National Natural Science Foundation of China (Grants Nos. 22302038, and 22202046) and the Minjiang Scholar Program of Fujian Province (Grants Nos. XRC-25069). The funders had no role in study design, data collection and analysis, decision to publish, or preparation of the manuscript.

Author contributions

Y.W. and J.L. conceived the paper. X.S. designed the experiments and analyzed the results. J.Z. performed the theoretical calculations. P.Z. conceived reaction mechanism. H.Zheng. and H.Zeng. assisted with materials characterizations. Y.J. and S.D. contribute to the STEM. P.W., N.W., Z.D., Z.Z., C.X., R.Y., W.D., and X.F. contributed to the data analysis and discussion. X.S., J.Z., P.Z., Y.W., X.F., and J.L. co-wrote the manuscript. All authors discussed the results and assisted during manuscript preparation.

Competing interests

The authors declare no competing interests.

Additional information

Supplementary information The online version contains supplementary material available at https://doi.org/10.1038/s41467-025-64389-9.

Correspondence and requests for materials should be addressed to Ying Wang or Jinlin Long.

Peer review information *Nature Communications* thanks Chiara Genovese, Lu Li and the other, anonymous, reviewer(s) for their contribution to the peer review of this work. A peer review file is available.